An update to this article is included at the end

Journal of Materials Research and Technology 39 (2025) 5573–5581

Contents lists available at ScienceDirect

Journal of Materials Research and Technology

journal homepage: www.elsevier.com/locate/jmrt

# Phase change material composites in a clay-like structure featuring GPTMS and butylated epoxy for heat buffering and thermal interface performance

Sangwoo Kim [a], Wondu Lee [a], Taeyoon Hwang [a], Jinhyun Park [a], Nahyun Lee [a], Pei-Chen Su [c], Jooheon Kim [a,b,*]

[a] School of Chemical Engineering, Chung-Ang University, Seoul, 06974, Republic of Korea
[b] Department of Intelligent Energy and Industry, Graduate School, Chung-Ang University, Seoul, 06974, Republic of Korea
[c] School of Mechanical and Aerospace Engineering, Nanyang Technological University, 50 Nanyang Avenue, 639798, Singapore

ARTICLE INFO

*Keywords:*
GPTMS
Lauric acid
Thermal conductivity
Latent heat
Skeleton
Heat buffering

ABSTRACT

Phase change material (PCM)-based thermal interface materials (TIMs) offer both heat conduction and buffering, but their practical use is hindered by leakage during phase transitions, discontinuous thermal pathways, and insufficient structural stability. Here, we report a clay-like PCM composite engineered by integrating (3-glycidyloxypropyl)trimethoxysilane (GPTMS)-functionalized boron nitride (BN) with a butylated epoxy (BuEP) matrix. GPTMS treatment enhanced interfacial compatibility between BN and lauric acid (LA), enabling efficient latent heat transfer and stable PCM retention. A continuous thermally conductive skeleton was formed by the aligned BN network impregnated with LA, while the BuEP matrix prevented leakage and improved mechanical robustness. The optimized composite achieved high thermal conductivity (5.68 W/m·K), significant latent heat storage (96.43 J/g), and excellent electrical insulation (>$10^{11}$ Ω cm), while maintaining mechanical compliance (elongation ~69 %). These properties translated into superior thermal regulation performance under device-level testing, demonstrating reduced temperature rise and stable operation. This study provides a practical design strategy that simultaneously addresses leakage, discontinuous conduction, and structural instability, thereby broadening the potential of PCM-based TIMs for next-generation electronic systems.

## 1. Introduction

Efficient thermal management has become increasingly important in modern compact electronic devices such as smartphones [1] and wearable systems [2] As devices continue to shrink and become more integrated, the heat generated per unit area rises significantly, often causing severe localized overheating. [3]. This thermal stress not only degrades device performance but also shortens the lifespan of critical components and compromises user comfort and safety.

To address these challenges, thermal interface materials (TIMs) [4] are commonly used to minimize thermal resistance between heat sources and heat sinks. TIMs fill microscopic interfacial voids between heat-generating components and heat dissipation structures, reducing contact resistance and facilitating heat transfer. However, conventional TIMs that rely solely on thermal conduction [5] often fail to buffer sudden temperature surges in high-power-density systems [6]. This limitation has increased demand for multifunctional TIMs with capabilities beyond simple conduction [7].

One promising approach involves incorporating phase change materials (PCMs) [8,9]into TIMs. A wide variety of PCMs have been explored for thermal management, including paraffin waxes (e.g., n-octadecane [10], n-eicosane [11], n-docosane [12]) known for their high latent heat and chemical stability; fatty acids (e.g., palmitic acid [13], myristic acid [14], stearic acid [15]) offering sharp phase transition temperatures and good compatibility with polymers; hydrated salts (e.g., sodium sulfate decahydrate [16], calcium chloride hexahydrate [17]) with high volumetric latent heat; and polymer-based solid–solid PCMs (e.g., polyethylene glycol [18], polyurethane [19]) that avoid leakage by maintaining a solid state throughout phase changes. PCMs absorb and release latent heat during phase transitions, providing temporary thermal storage and enhancing thermal buffering. Lauric acid [20–22], with a phase transition temperature of approximately 43–46 °C, is particularly well-suited for mitigating transient thermal spikes in smartphones, wearables, and PC CPUs, which frequently exceed 50 °C during intensive use or charging.

However, most existing PCM-based TIMs rely on simple physical

* Corresponding author. School of Chemical Engineering, Chung-Ang University, Seoul, 06974, Republic of Korea.
*E-mail address:* jooheonkim@cau.ac.kr (J. Kim).

https://doi.org/10.1016/j.jmrt.2025.10.218
Received 10 September 2025; Received in revised form 22 October 2025; Accepted 26 October 2025
Available online 27 October 2025
2238-7854/© 2025 The Authors. Published by Elsevier B.V. This is an open access article under the CC BY-NC-ND license (http://creativecommons.org/licenses/by-nc-nd/4.0/).

blending of PCM and thermally conductive fillers, resulting in poor interfacial contact and discontinuous thermal pathways. These structural limitations hinder the efficient release of stored thermal energy and ultimately degrade overall thermal performance. To prevent PCM leakage and maintain structural integrity during phase transitions, a stabilizing matrix is essential. If the matrix is too soft, it may fail to retain the PCM; if too rigid, it may reduce interfacial contact with the heat source and hinder thermal conduction.

In this study, a novel TIM composite design is proposed to simultaneously address PCM leakage, discontinuous thermal pathways, and mechanical instability. Hydroxyl groups were first introduced onto the surface of hexagonal boron nitride (h-BN [23,24]), followed by silanization with 3-glycidyloxypropyltrimethoxysilane (GPTMS [25]) to enhance interfacial reactivity and compatibility with both the PCM and the matrix materials.

GPTMS undergoes hydrolysis to form silanol groups, which covalently bond to hydroxylated BN surfaces through condensation reactions, resulting in stable surface anchoring. The epoxide terminal group of GPTMS subsequently interacts with the carboxyl group of lauric acid through hydrogen bonding or chemical reaction, significantly enhancing interfacial compatibility between the filler and PCM. This dual interfacial activity plays a crucial role in improving PCM retention, dispersion stability, and the continuity of the thermal conduction network.

The functionalized BN was assembled into a directionally aligned, continuous thermal conduction skeleton in the form of an aerogel, which was impregnated with lauric acid to enable latent heat storage. A butylene-based, high-thermal-conductivity epoxy matrix was subsequently introduced to suppress PCM leakage and enhance mechanical integrity.

The epoxy used in this study features a bisphenol A backbone modified with flexible ether and alkyl chains, offering higher thermal conductivity and flexibility than conventional DGEBA-based epoxies [26]. This molecular structure improves compatibility with both the filler and the PCM, reduces internal stress concentrations, and enhances the stability of the thermal conduction network [27,28].

Finally, the composite was cured under high temperature and pressure using a hot-pressing process to ensure complete crosslinking of the epoxy matrix and to enhance interfacial contact and mechanical cohesion.

## 2. Experimental section

### 2.1. Materials

Hexagonal boron nitride (BN; average particle size ~12 μm, Momentive Performance Materials, USA) was used as the thermally conductive filler. Lauric acid (LA; synthesis grade, Sigma-Aldrich) served as the phase change material (PCM). (3-Glycidyloxypropyl)trimethoxysilane (GPTMS; 98 %, Sigma-Aldrich) was used as the silane coupling agent. Cellulose nanofiber (CNF; 1 wt% aqueous suspension, CNNT Co., Korea) functioned as both a dispersant and structural binder. Butylated epoxy resin (BuEP; Epoxy Technology Inc., USA) was selected as the matrix for its intrinsic flexibility and higher thermal conductivity compared to conventional bisphenol-A-based epoxies. The resin exhibits a viscosity of 40,000–70,000 cPs at 23 °C (5 rpm). And the system is formulated as a two-component epoxy with a recommended mixing ratio of 100:15 by weight (Part A: Part B), which governs its curing behavior and interfacial bonding characteristics. Codeway CPU Thermal grease (commercial thermal paste; Codeway, Korea) was used as a reference material for comparison in the CPU core tests.

### 2.2. Hydroxylation and silanization of BN

Fig. 1 schematically illustrates the fabrication process of the GPTMS-functionalized BN/LA skeleton and its encapsulation in a BuEP matrix. To introduce hydroxyl groups, 1 g of BN was dispersed in 80 mL of deionized (DI) water containing 9.6 g of NaOH (3 M). The mixture was magnetically stirred for 30 min and sonicated using a tip sonicator for 1 h. The suspension was filtered, and the base treatment process was repeated twice. The resulting product was washed with DI water until the pH was neutral, and then dried to obtain hydroxylated BN (BN–OH).

For silanization, 0.6 mL of GPTMS and a small amount of acetic acid were added to 80 mL of ethanol. The pH was adjusted to approximately 5.5, and the solution was stirred at room temperature for 30 min. Subsequently, 1 g of BN–OH was added, and the reaction was carried out at 70 °C under reflux for 8 h with magnetic stirring. The GPTMS-functionalized BN (gBN) was collected by filtration, rinsed with deionized water and ethanol, and dried at 60 °C.

### 2.3. Fabrication of thermal conduction skeleton

To construct the thermal conduction skeleton, 1 g of gBN was added to 20 mL of a 1 wt% CNF suspension. The mixture was bath-sonicated for 30 min and magnetically stirred for 2 h to ensure uniform dispersion. The resulting suspension was cast into a 60 mm Petri dish and freeze-

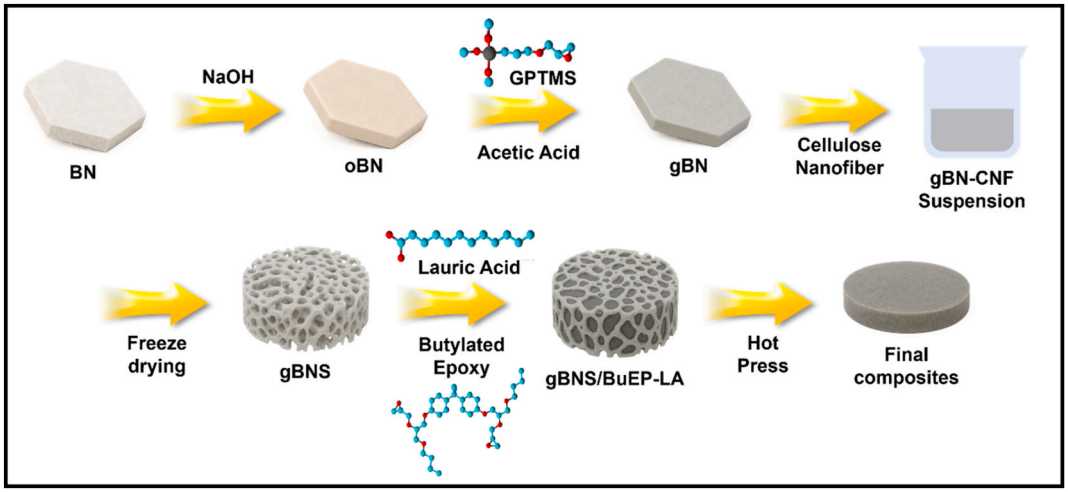



**Fig. 1.** Fabrication process of GPTMS-functionalized BN/LA skeleton and its encapsulation in a BuEP matrix.

dried for 48 h to obtain a porous aerogel with an interconnected gBN/CNF network.

### 2.4. Preparation of composite structure

LA melted at 80 °C in an oil bath. BuEP was added and manually mixed for 5 min, after which the curing agent was introduced and the mixture was stirred for an additional 5 min. The resulting mixture was immediately cast onto the gBN skeleton placed in a Petri dish, ensuring complete infiltration. Hot-pressing was conducted at 80 °C for 2 h to enable simultaneous infiltration and curing. Infiltration was performed promptly after mixing to maintain fluidity and prevent premature curing.

### 2.5. Characterization

Fourier-transform infrared spectroscopy (FT-IR) was used to identify functional groups and confirm chemical modifications. X-ray photoelectron spectroscopy (XPS) was performed to analyze elemental composition and bonding states. Field-emission scanning electron microscopy (FE-SEM) was used to examine surface morphology and microstructural features. Energy-dispersive X-ray spectroscopy (EDS) was employed to assess elemental distribution. Laser flash analysis (LFA) was conducted to measure thermal conductivity. Differential scanning calorimetry (DSC) was used to evaluate latent heat and phase transition behavior. Volume resistivity was measured using the four-point probe method. Mechanical properties, including tensile strength and elongation, were evaluated using a universal testing machine (UTM).

## 3. Results and discussion

### 3.1. Skeleton analysis

Fig. 2 summarizes the spectroscopic evidence supporting the sequential surface modification of BN through hydroxylation and GPTMS functionalization. This analysis provides direct molecular-level evidence supporting the surface-engineering strategy that underpins the improved interfacial compatibility and thermal transport behavior demonstrated later in the composite system. Fig. 2(a) shows the stepwise functionalization of BN with GPTMS. Pristine BN was first hydroxylated under alkaline conditions to produce hydroxylated BN (oBN) with –OH groups covalently bound to B sites. These hydroxyl groups then reacted with the methoxy groups of (3-glycidyloxypropyl)trimethoxysilane (GPTMS) via condensation, yielding GPTMS-functionalized BN (gBN) with epoxy-terminated organosilane chains. The resulting organosilane layer acts as a "bridge" that promotes chemical and physical interactions between BN and lauric acid, thereby greatly enhancing their interfacial compatibility. Fig. 2(b) shows the FT-IR spectra of BN, oBN, and gBN. In the BN spectrum, characteristic peaks at ~1365 $cm^{-1}$ and ~800 $cm^{-1}$ are assigned to B–N stretching and B–N–B bending vibrations, respectively. The oBN sample exhibits a broad O–H stretching peak near 3430 $cm^{-1}$, confirming the introduction of hydroxyl groups via NaOH treatment. GPTMS contains methoxy groups capable of hydrolyzing to silanols, which can condense with surface –OH groups on oBN to form covalent Si–O–B linkages. Its epoxy terminal groups can further promote interfacial interactions with both LA and the BuEP matrix. In the gBN spectrum, peaks at 1100–1030 $cm^{-1}$ correspond to Si–O–Si and Si–O–C stretching, while a weaker band at 950–910 $cm^{-1}$ originates from epoxide ring vibrations, indicating successful grafting of GPTMS onto the BN surface. Additional bands near 2930 $cm^{-1}$ and 2850 $cm^{-1}$ are attributed to $–CH_2–$ stretching, and the feature at ~1250 $cm^{-1}$ corresponds to C–O–C stretching, both originating from the GPTMS organic

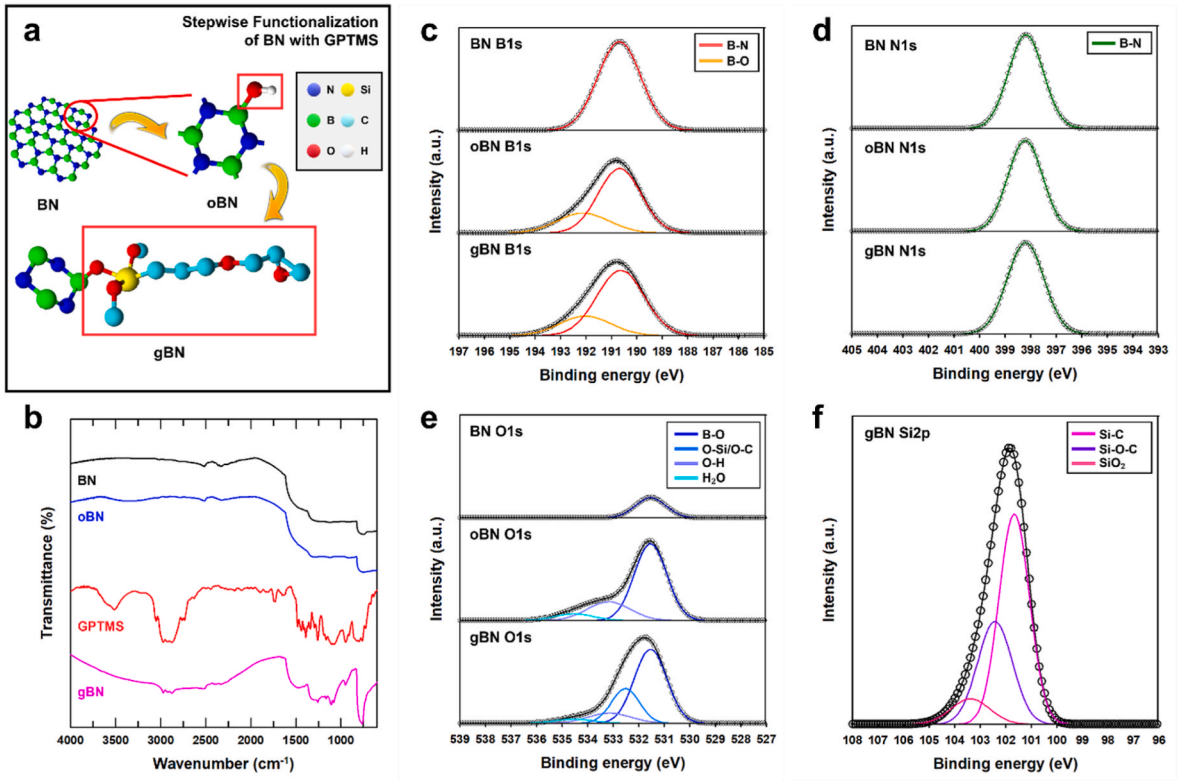



**Fig. 2.** Spectroscopic characterization confirming the sequential surface modification of BN through hydroxylation and GPTMS functionalization. (a) Schematic illustration of the stepwise functionalization process from BN to oBN and gBN. (b) FT-IR spectra of BN, oBN, GPTMS, and gBN. (c) B 1s XPS spectra, (d) N 1s XPS spectra, (e) O 1s XPS spectra of BN, oBN, gBN. (f) Si 2p XPS spectra of gBN.

moieties. Compared with oBN, the O–H band intensity in gBN is notably reduced, suggesting consumption of surface hydroxyls during silanization. The spectral evolution supports the two-step surface functionalization process, collectively confirming the sequential introduction of hydroxyl groups and GPTMS moieties onto the BN surface, which lays the chemical foundation for constructing a well-bonded gBN–BuEP interface with enhanced phonon transport and phase-change stability. Fig. 2(c) shows the B 1s XPS spectra. Pristine BN shows a peak at ~190.2 eV, attributed to B–N bonds. After hydroxylation, oBN displays an additional peak at ~191.2 eV, corresponding to B–O bonds, confirming the introduction of surface hydroxyl groups. In gBN, the B–O component persists, indicating that the hydroxylated sites remain partially present after silanization with GPTMS. Fig. 2(d) shows the N 1s XPS spectra. All samples exhibit a dominant peak at ~398.2 eV, corresponding to B–N bonds in hexagonal BN. No significant peak shifts or additional features are observed after hydroxylation or GPTMS treatment, indicating that the nitrogen chemical environment remains stable throughout the surface modification process. Fig. 2(e) shows the O 1s XPS spectra. In BN, the O 1s peak appears weak and is mainly assigned to B–O bonds at ~531.5 eV. After hydroxylation, oBN exhibits a much stronger O 1s signal with pronounced B–O (~531.5 eV) and O–H (~533.2 eV) components, as well as a minor feature at ~534–535 eV attributed to adsorbed $H_2O$, confirming the formation of surface hydroxyl groups. In gBN, an additional O–Si/O–C component emerges at ~532.5 eV, which is consistent with the formation of covalent Si–O–B and Si–O–C linkages after GPTMS treatment. The O–H contribution decreases compared with oBN, indicating consumption of hydroxyl groups during silanization. Fig. 2(f) shows the Si 2p XPS spectrum of gBN. The spectrum can be deconvoluted into three components: Si–C at ~101.5 eV, Si–O–C at ~102.5 eV, and a minor $SiO_2$-related peak at ~103.5 eV. The Si–O–C and Si–C signals originate from the covalent bonding of GPTMS to the hydroxylated BN surface, while the $SiO_2$ peak likely arises from partial oxidation of silane moieties during processing. These results further confirm the successful grafting of GPTMS onto BN, thereby validating the sequential modification route proposed in Fig. 2(a) and reinforcing the chemical rationale of our composite design.

Fig. 3 presents morphological and compositional analyses supporting the surface modification of BN and the formation of the gBN-based thermal conduction skeleton. Fig. 3(a) shows the FE-SEM image of BN, revealing its characteristic layered structure typical of a hexagonal crystal system. In Fig. 3(b), the surface of gBN appears slightly roughened, indicating subtle changes associated with surface functionalization. Fig. 3(c–e) provide EDS data confirming the presence of B, in addition to N and Si, in gBN, supporting the successful grafting of GPTMS onto the BN surface. Fig. 3(f) presents a macroscopic image of the freeze-dried gBN-based skeleton, showing a porous and interconnected structure designed to facilitate directional heat transfer and improve interfacial contact with the infiltrated PCM. Fig. 3(g) further confirms this morphology through FE-SEM imaging, clearly revealing interconnected BN platelets forming a continuous porous skeleton architecture.

### 3.2. Binding matrix analysis

Fig. 4 presents FT-IR and FE-SEM analyses of the binding matrix, focusing on lauric acid (LA), butylated epoxy (BuEP), and their mixture (LA–BuEP). Fig. 4(a) shows the FT-IR spectra of LA, BuEP, and their mixture (LA–BuEP). LA exhibits a strong C═O stretching band at ~1690 $cm^{-1}$ and a broad O–H stretching band near ~3300 $cm^{-1}$. BuEP displays a characteristic epoxide ring vibration at ~910 $cm^{-1}$ along with typical C–O–C stretching bands. In LA–BuEP, the C═O band of LA shifts and the O–H band broadens, while the epoxide peak of BuEP is markedly reduced, indicating partial ring-opening reactions between the epoxy groups of BuEP and the carboxyl groups of LA. These spectral changes confirm chemical interactions and hydrogen bonding at the LA/BuEP interface. Fig. 4(b) presents the FE-SEM image of raw LA, showing

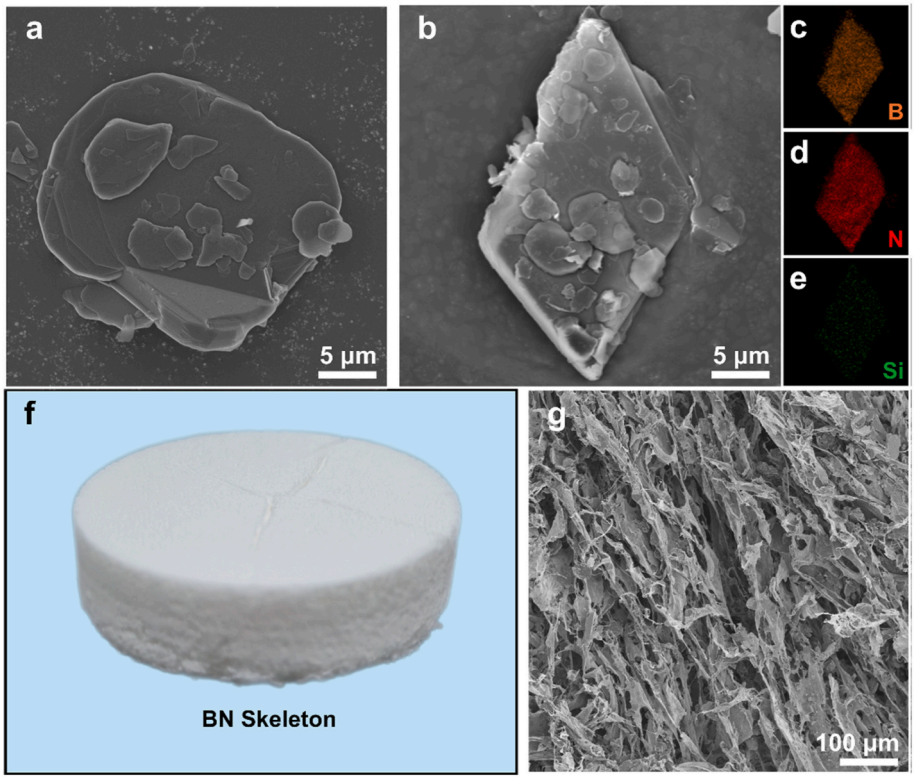



**Fig. 3.** Morphological and compositional characterization of BN and the gBN-based skeleton. (a) FE-SEM image of BN. (b) FE-SEM image of gBN after GPTMS functionalization. (c–e) EDS mapping of gBN showing B, N, and Si. (f) Macroscopic image of the freeze-dried gBN-based skeleton. (g) FE-SEM image of the skeleton showing interconnected BN platelets.

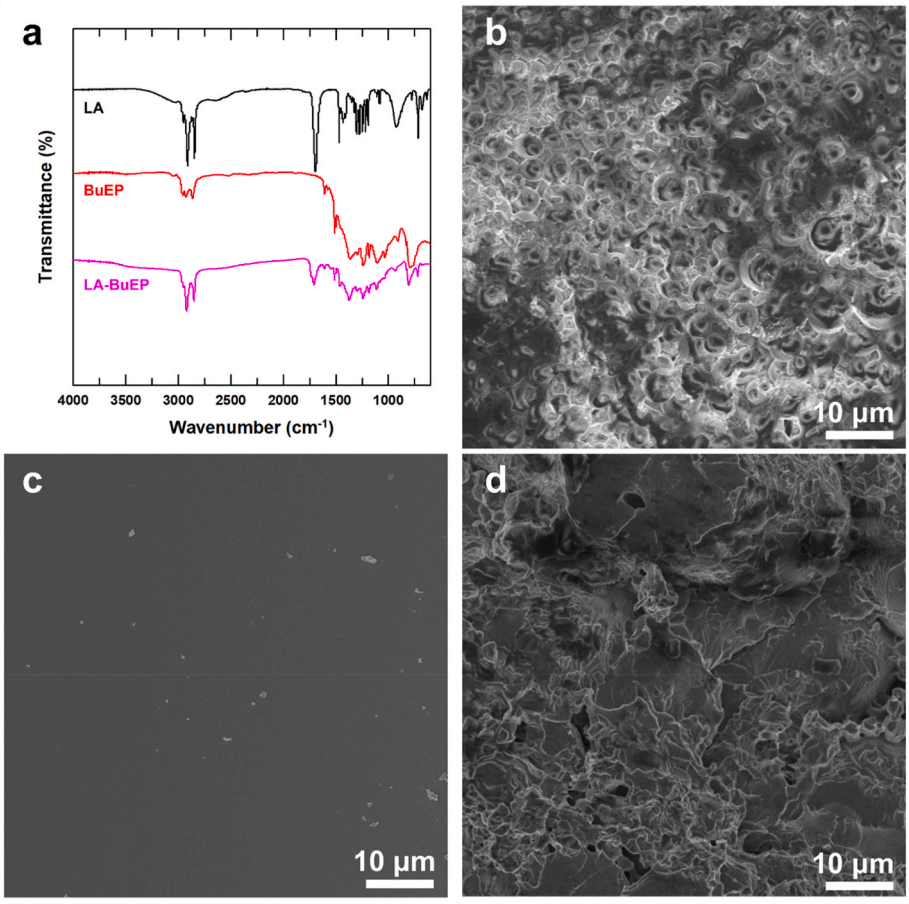



**Fig. 4.** (a) FT-IR spectra of LA, BuEP, and LA–BuEP. (b–d) FE-SEM images of (b) raw LA, (c) neat BuEP, and (d) LA–BuEP mixture.

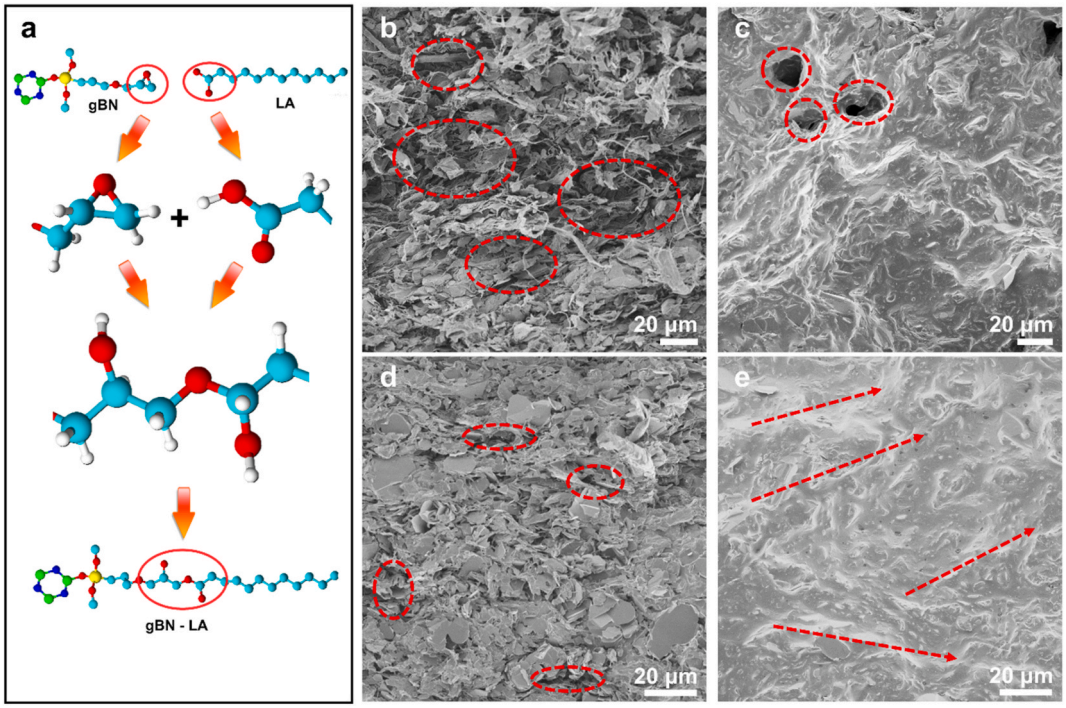



**Fig. 5.** (a) Proposed reaction mechanism between gBN and LA. (b–e) FE-SEM images of fracture surfaces: (b) BN–EP, (c) gBN–EP, (d) BN–BuEP, and (e) gBN–BuEP.

densely packed crystalline domains with irregular edges, characteristic of solid-state lauric acid. These aggregated plate-like crystals are expected to undergo melting and morphological rearrangement upon heating during PCM integration. Fig. 4(c) shows neat BuEP with a smooth, featureless surface and only a few scattered particulates, indicating the absence of significant microstructural features and reflecting the homogeneous nature of the butylated epoxy matrix prior to PCM incorporation. Fig. 4(d) depicts the LA–BuEP mixture, revealing a rough and heterogeneous surface with irregular domains and interfacial features, suggesting partial integration of LA within the BuEP matrix, consistent with the chemical interactions observed in FT-IR analysis.

### 3.3. Composites analysis

Fig. 5 presents the interfacial interaction mechanism between gBN and LA, along with comparative FE-SEM analyses of composite morphologies as a function of BN surface treatment and epoxy matrix type. Fig. 5(a) illustrates the proposed reaction mechanism between gBN and LA. The epoxy groups on the GPTMS layer of gBN undergo a ring-opening reaction [29] with the carboxyl groups of LA, forming covalent ester linkages. This chemical bonding enhances interfacial compatibility, serves as an efficient thermal bridge to transfer latent heat stored in LA, and effectively mitigates PCM leakage during phase transition. Fig. 5(b–e) present FE-SEM images of composites with different BN surface treatments and epoxy matrices. In Fig. 5(b), the BN–EP composite, containing untreated BN and a bisphenol-A-based epoxy matrix, exhibits poor interfacial adhesion and a rough, discontinuous morphology, as marked by the red circles indicating interfacial gaps and filler agglomeration. In Fig. 5(c), gBN–EP shows improved interfacial bonding with the epoxy matrix compared to (b), although the inherent rigidity of the bisphenol-A-based epoxy results in a somewhat uneven interface, with several voids still visible. Fig. 5(d) shows the BN–BuEP composite, where the absence of BN surface treatment still limits interfacial integration, but the higher flexibility of the butylated epoxy yields a more conformal contact than in (b), as indicated by the reduced number of voids. In contrast, the gBN–BuEP composite in Fig. 5 (e) demonstrates both strong interfacial bonding and smooth morphological integration, as highlighted by the red arrows showing continuous BN alignment, enabling the formation of uninterrupted thermal conduction pathways and ensuring excellent interfacial cohesion.

Fig. 6(a) illustrates the thermal regulation mechanism and performance of the composites, encompassing their heat management concept, morphological stability under stepwise heating, thermal conductivity, and latent heat storage capacity. In the “before heat absorption” state (left), the gBN skeleton forms continuous thermal pathways that enable rapid heat transport, while LA is uniformly distributed along the GPTMS-functionalized BN surface. In the “after heat absorption” state (right), the embedded LA stores thermal energy via latent heat absorption during its phase transition. This synergy between the highly conductive gBN network and the phase-change LA ensures both efficient heat dissipation and transient thermal buffering. Systems relying solely on conduction fail to suppress temperature spikes, whereas those based only on phase-change mechanisms cannot sustain heat dissipation. The integration of gBN and LA thus overcomes both limitations, providing stable thermal regulation under dynamic thermal loads. In addition, the flexible BuEP matrix reduces interfacial air voids and maintains intimate contact with the filler and heat source, further enhancing overall heat transfer. Fig. 6(b) shows the quantitative leakage evaluation of the composite under stepwise heating. Each sample was heated from 30 °C to 150 °C at 10 °C intervals and maintained for 15 min at each step, followed by weight measurement. The gBN–BuEP composite retained 98.74 % of its initial weight up to 100 °C, and this minor reduction was attributed to the adhesive nature of the sample rather than actual leakage. At 110 °C, the sample showed a noticeable decrease to 97.71 %,

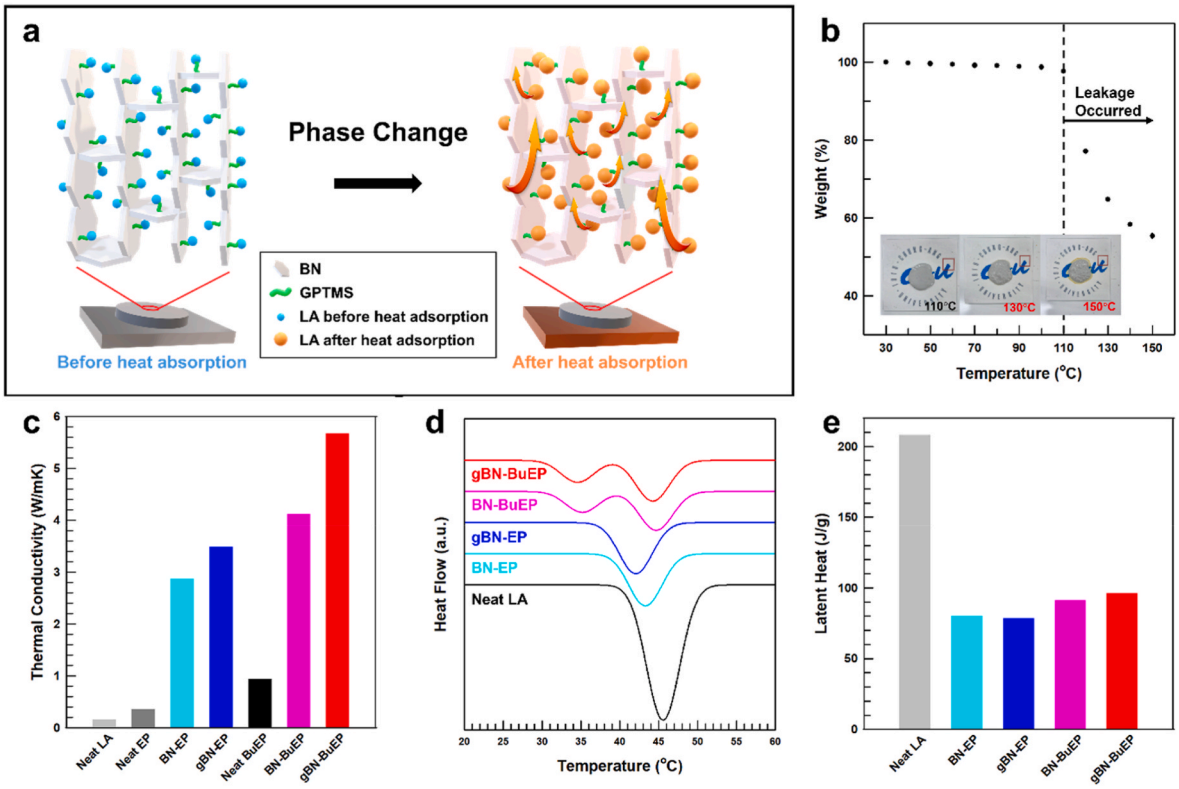



**Fig. 6.** (a) Synergistic thermal management mechanism of the gBN–LA–BuEP composite, integrating thermal conduction and latent heat storage. (b) Leakage test of the gBN–BuEP composite under stepwise heating from 30 °C to 150 °C. (c) Thermal conductivity of neat matrices and BN/gBN composites. (d) DSC curves of neat LA and composites. (e) Latent heat capacities showing effects of BN functionalization and matrix type.

although no visible wetting of the supporting paper was detected. Above 110 °C, the mass loss accelerated sharply, and the residual weight dropped to 55.42 % at 150 °C, indicating that most of the encapsulated LA (50 wt %) had leaked out. These quantitative results clearly confirm that the composite remains leakage-free and structurally stable up to approximately 100 °C, ensuring safe use under typical thermal management conditions. Fig. S1 shows the thermogravimetric analysis (TGA) results of the neat components and the gBN–BuEP composite under $N_2$ atmosphere. Neat LA exhibited a complete mass loss between 180 and 330 °C, whereas neat BuEP retained ~20 wt% residue after decomposition in the range of 320–480 °C. As expected, neat BN remained thermally stable without appreciable weight loss up to 800 °C. The gBN–BuEP composite showed a characteristic two-step degradation corresponding to the volatilization of LA and the decomposition of BuEP, leaving ~31 wt% residue at 800 °C due to the presence of BN and carbonaceous char [30,31]. These results corroborate the morphological observations in Fig. 6(b), confirming that the composite not only preserves its shape under operating conditions (<110 °C) but also possesses an inorganic skeleton that enhances thermal stability against high-temperature decomposition. Fig. 6(c) compares the thermal conductivities of the composites and their respective matrices. The thermal conductivity (k) of the composites was determined using the well-established relation

$$k = \alpha \times Cp \times \rho$$

where α is the thermal diffusivity ($cm^2\ s^{-1}$), $C_p$ is the specific heat capacity ($J\ g^{-1}\ K^{-1}$), and ρ is the bulk density ($g\ cm^{-3}$). Both α and $C_p$ were measured simultaneously using laser flash analysis (LFA), while the density (ρ) of each composite was determined directly from its mass-to-volume ratio. The obtained values of α, $C_p$, ρ, and the calculated k are summarized in Table S1, providing the complete set of parameters used for thermal conductivity evaluation. Neat LA, EP and BuEP exhibited low conductivities of 0.16, 0.36 and 0.94 W/m·K, respectively. Incorporating untreated BN increased these values to 2.88 W/m·K (BN–EP) and 4.12 W/m·K (BN–BuEP), while GPTMS-functionalized BN (gBN) further enhanced them to 3.49 W/m·K (gBN–EP) and 5.68 W/m·K (gBN–BuEP). These results indicate that both BN surface functionalization and matrix selection contribute to thermal conductivity improvement, with gBN–BuEP achieving the highest performance through the synergistic effects of improved interfacial bonding and the relatively higher intrinsic conductivity of BuEP. While surface functionalization primarily benefits thermal conductivity, its influence on phase change behavior is limited. Instead, the flexibility of BuEP plays a more decisive role in latent heat retention by reducing constraints on LA crystallization and recrystallization. Fig. 6(d) and (e) then evaluate the latent heat performance of the composites. As shown in Fig. 6(d), all composites exhibit lower latent heat and a slight shift of the melting peak toward lower temperatures compared to neat LA, with gBN-containing systems displaying a more pronounced shift. This behavior can be attributed to interfacial confinement effects introduced by GPTMS functionalization [32]. Supporting evidence is provided by the FT-IR spectrum in Fig. 2 (b), where gBN exhibits characteristic Si–O–Si and Si–O–C stretching bands, confirming the successful grafting of GPTMS onto BN. These polar groups enhance compatibility with the BuEP matrix and promote stronger interactions with LA molecules, which restrict lamellar growth in the interfacial regions. The resulting reduction in lamellar thickness induces a Gibbs–Thomson-type depression of the phase transition temperature [33], thereby accounting for the observed left shift in the DSC peak. In addition, the split melting peak was observed only in BuEP-based samples, whereas EP-based composites exhibited a single peak. This difference can be ascribed to the more flexible and less polar nature of BuEP, which facilitates the coexistence of two distinct LA domains: a confined fraction strongly interacting with the filler–matrix interface and a bulk-like fraction residing in larger free volumes [34]. In contrast, the more rigid bisphenol-A epoxy matrix provides a more uniform environment for LA, resulting in a single melting transition. The more pronounced low-temperature component in gBN–BuEP further supports this interpretation, consistent with the enhanced interfacial interactions confirmed by the FT-IR results in Fig. 2(b) [35]. This pronounced low-temperature shift in the gBN–BuEP system originates from the synergistic interfacial confinement induced by GPTMS functionalization and the flexible BuEP matrix. The strong polar interactions at the GPTMS-modified BN surface, coupled with the enhanced molecular mobility of BuEP, cooperatively expand the confined LA fraction, leading to a more significant depression of the phase transition temperature [36]. Fig. 6(e) quantifies the latent heat values, revealing that gBN–BuEP (96.43 J/g) achieves the highest among the composites, although still lower than neat LA (208.24 J/g) due to the reduced PCM fraction caused by the incorporation of the BN skeleton and epoxy matrix. While surface functionalization slightly affects phase transition behavior, the matrix material exerts a stronger influence, as BuEP-based systems (gBN–BuEP: 96.43 J/g; BN–BuEP: 91.58 J/g) generally show higher latent heat than their bisphenol-A-based epoxy counterparts (gBN–EP: 78.55 J/g; BN–EP: 80.12 J/g). Notably, BN–EP even surpasses gBN–EP in latent heat, indicating that the flexibility of the matrix plays a more decisive role than BN surface functionalization itself. In addition, Fig. S2 compares the thermal conductivity and latent heat of this work with previously reported PCM composites, showing that the present gBN–BuEP system exhibits excellent thermal conductivity while maintaining a substantial latent heat capacity. Fig. S3 further demonstrates the cycling reliability of the composites, where the latent heat of gBN–BuEP decreased only slightly from 96.43 J/g before cycling to 91.03 J/g after 50 cycles (20–90 °C), corresponding to a mere 5.6 % reduction, while the melting temperature remained nearly unchanged within ±1 °C. This result highlights the excellent long-term thermal reliability of the developed system.

### 3.4. Application test

Fig. 7(a) demonstrates the strong adhesive properties of the gBN–LA–BuEP composite. When a flat plastic plate was pressed onto the sample and then lifted, the composite was pulled upward and elongated due to its high tackiness, without any visible cracking or delamination. This continuous elongation confirms the material's mechanical compliance. Such behavior is attributed to the influence of the flexible butylated epoxy matrix and lauric acid chains, rendering the composite well-suited for thermal interface applications that require stable adhesion to irregular or moving surfaces. The incorporation of GPTMS-treated BN improves interfacial compatibility, enhancing adhesion and ensuring long-term mechanical stability under repeated stress or thermal cycling. Fig. 7(b) and (c) present the tensile stress–strain behavior and corresponding mechanical properties. The gBN–BuEP composite exhibited a higher tensile strength than BN–BuEP (17.89 MPa vs. 11.24 MPa), but its elongation (69.12 %) was lower than that of BN–BuEP, which showed the highest value among all samples (82.35 %). In contrast, EP-based composites (gBN–EP and BN–EP) displayed much higher tensile strengths (78.56 MPa and 63.78 MPa, respectively) but very limited elongations (4.12 % and 4.94 %, respectively). The superior stretchability of BuEP-based composites is advantageous for accommodating thermal expansion and mechanical deformation, thereby reducing the risk of delamination or cracking. This flexibility also enhances conformity to curved or irregular surfaces, lowering interfacial thermal resistance and facilitating integration with complex device geometries. Fig. 7(d) confirms the excellent electrical insulation of all composites, with volume resistivity values exceeding $10^9$ Ω cm. This behavior arises from the intrinsic insulating nature of BN, BuEP, and LA, which do not form conductive pathways. The CPU thermal performance test consisted of three consecutive stages: a 100-s idle monitoring period, a 400-s full-load stress test, and a subsequent 100-s cooling stage. Fig. 7(e) and (f) present the CPU core temperature and effective core clock profiles, respectively, over the duration of the thermal stress test.

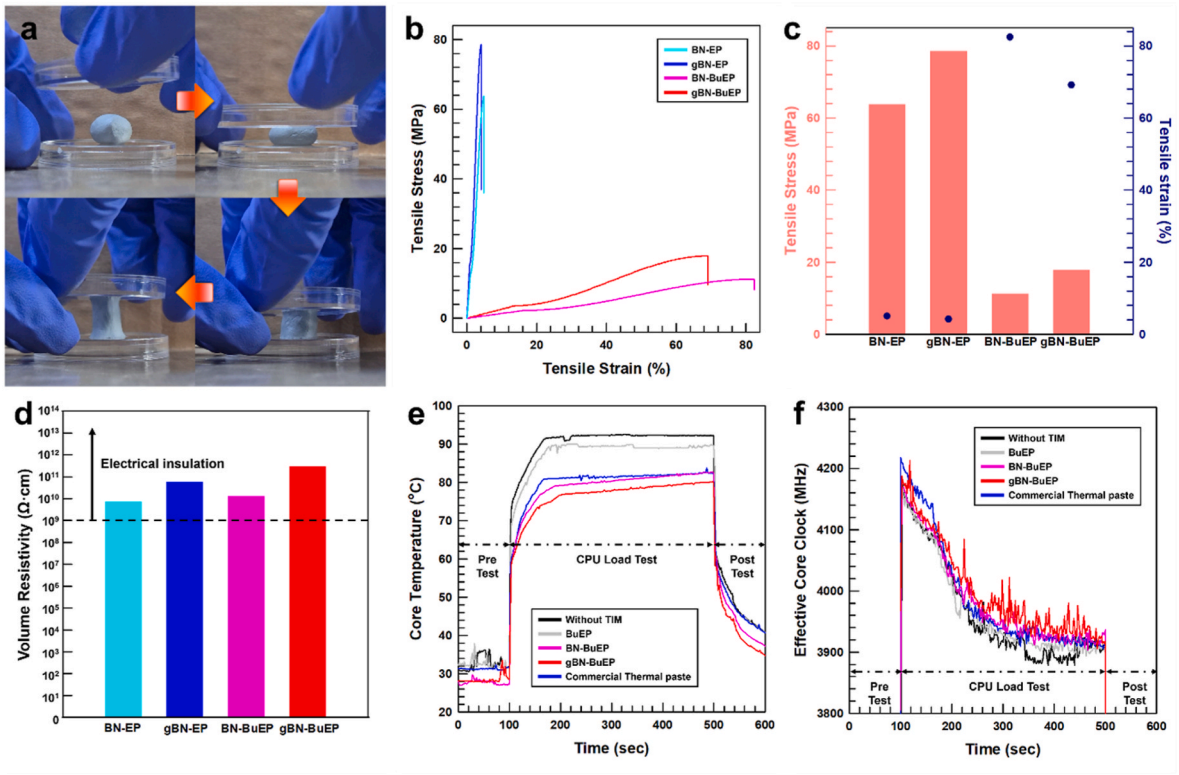



**Fig. 7.** (a) Adhesive behavior of the gBN–BuEP composite under tack test. (b, c) Tensile stress–strain curves and corresponding mechanical properties. (d) Volume resistivity of composites. (e) CPU core temperature profiles during CPU core test. (f) Effective core clock frequencies corresponding to temperature profiles in (e).

As shown in Fig. 7(e), the gBN–BuEP composite achieved the lowest peak core temperature (80.1 °C), followed by BN–BuEP (82.7 °C), the commercial thermal paste (83.8 °C), BuEP (89.8 °C), and the no-TIM condition (92.4 °C). Both gBN–BuEP and BN–BuEP exhibited a delayed temperature rise during heating, demonstrating a distinct heat-buffering effect originating from the latent-heat absorption of LA, whereas the commercial thermal paste showed a more immediate temperature increase without such buffering behavior. Specifically, the commercial paste reached 80 °C within only 162 s and quickly stabilized around 82–83 °C, indicating a rapid saturation of heat transfer across the interface. In contrast, the BN–BuEP sample required approximately 262 s to reach the same temperature despite having a comparable peak value, clearly evidencing its thermal-buffering capability. The gBN–BuEP composite showed an even more gradual temperature increase with a sustained upward slope, highlighting the combined effect of the GPTMS-modified interface and the latent-heat absorption of LA in retarding the temperature rise. This temperature moderation is attributed to the strong interfacial bonding between BN and LA via GPTMS, which enables efficient heat transfer from LA—during latent heat absorption—to the high-thermal-conductivity BN skeleton. As shown in Fig. 7(f), samples with lower core temperatures consistently maintained higher effective core clock frequencies. In particular, the gBN–BuEP composite sustained the highest average clock frequency among all samples, demonstrating its practical applicability as a high-performance TIM. Consequently, the gBN–BuEP composite enables stable high-performance operation through effective suppression of temperature rise during heavy computational loads.

Fig. S4 illustrates the schematic diagram and actual setup of the CPU core testing used to evaluate the practical heat-dissipation performance of the composites. The schematic provides an overview of the measurement configuration, showing the CPU, the applied thermal-interface layer, and the mounted heatsink–fan assembly. The accompanying photographs depict the test procedure, where either gBN–BuEP or the commercial thermal paste was uniformly applied onto the CPU surface, followed by installation of the heatsink and cooling fan. The tests were performed using an Intel® Core™ i3-10100 processor operating at its stock frequency, with a full-load power of approximately 80 W applied through OCCT (OverClock Checking Tool) for 20 min. HWiNFO64 was used for real-time temperature monitoring and data acquisition. This schematic and photographic representation clarifies the experimental configuration and confirms that all samples were tested under identical conditions.

## 4. Conclusion

In this study, a multifunctional phase change composite was engineered by integrating gBN, LA, and a BuEP matrix. Central to its performance is the use of GPTMS, which provided strong chemical coupling between BN and LA, enabling efficient latent heat transfer to the thermally conductive BN skeleton and ensuring stable PCM retention. This interfacial engineering yielded a robust and continuous heat conduction framework, maximizing the synergy between thermal conductivity and latent heat capacity. BuEP, rarely applied in conventional TIMs, was selected for its inherently higher thermal conductivity and superior flexibility, which improved compatibility with heat sources and reduced interfacial thermal resistance—a factor often overlooked in previous studies.

The resulting composite exhibited a rare combination of high thermal conductivity, substantial latent heat capacity, mechanical compliance, and excellent electrical insulation. By uniting GPTMS-driven interfacial optimization with BuEP's mechanical adaptability, this design strategy addresses both thermal and mechanical reliability requirements, offering a promising route toward next-generation TIMs.

Importantly, this work directly addresses the three critical challenges outlined in the introduction: (i) PCM leakage is effectively suppressed below 110 °C by the BuEP matrix and the filler-supported framework; (ii) discontinuous thermal conduction is mitigated through the formation of a continuous gBN skeleton coupled with GPTMS-enabled

interfacial bonding; and (iii) structural instability is alleviated by the clay-like composite architecture, which combines mechanical compliance with dimensional stability during cycling. Furthermore, the clay-like structure provides overall tackiness and adaptability that enable the composite to effectively fill interfacial voids between the TIM and heat source, thereby minimizing contact thermal resistance.

Nevertheless, it should be noted that the present composite remains stable mainly around 40–50 °C but shows leakage at elevated temperatures above 110 °C. This limitation also points to a clear path for future improvements, with higher-melting PCMs, encapsulation strategies, and matrix optimization expected to extend the design concept toward broader operating windows and more demanding thermal management applications.

## Declaration of competing interest

The authors declare that they have no known competing financial interests or personal relationships that could have appeared to influence the work reported in this paper.

## Acknowledgments

This research was supported by On-site Customized Personal Protection Technology Based on Multilayer Advanced Materials Program through the Korea Institutes of Police Technology (KIPoT) funded by the Korean National Police Agency & the National Fire Agency* (No. RS-2025-02221259)

## Appendix A. Supplementary data

Supplementary data to this article can be found online at https://doi.org/10.1016/j.jmrt.2025.10.218.

## References

[1] Hu T, Zhang J, Chan W, Xiao R, Xu H, Zhao X, et al. Synthesis and optimization of GO/TiO2@n-octadecane microcapsules for thermal management of smartphone charging. Appl Therm Eng 2024;257. https://doi.org/10.1016/j.applthermaleng.2024.124409.

[2] Kurhade AS, Siraskar GD, Bhambare PS, Kaithari DK, Dixit SM, Waware SY. Enhancing smartphone circuit cooling: a computational study of PCM integration. J Adv Res Numerical Heat Trans 2024;27:132–45. https://doi.org/10.37934/arnht.27.1.132145.

[3] Shahid S, Agelin-Chaab M. A review of thermal runaway prevention and mitigation strategies for lithium-ion batteries. Energy Convers Manag X 2022;16. https://doi.org/10.1016/j.ecmx.2022.100310.

[4] Wei B, Luo W, Du J, Ding Y, Guo Y, Zhu G, et al. Thermal interface materials: from fundamental research to applications. SusMat 2024;4. https://doi.org/10.1002/sus2.239.

[5] Han Y, Ruan K, He X, Tang Y, Guo H, Guo Y, et al. Highly thermally conductive aramid nanofiber composite films with synchronous visible/infrared camouflages and information encryption. Angew Chem, Int Ed 2024;63. https://doi.org/10.1002/anie.202401538.

[6] Liang G, Zhang X, Zhao J, Geng L, Lin Y, Liu Y, et al. Intrinsic flame-retardant solid–solid organic phase change materials for high-security thermal management. Small 2025;21. https://doi.org/10.1002/smll.202503431.

[7] Kim J, Jang E, Cho J, Kim J. Iron oxide/magnesium oxide/graphene oxide/cellulose composites with superior thermal conductivity, EMI shielding, and electrical insulation synthesis using polydopamine linker. ACS Appl Polym Mater 2024;6:8775–85. https://doi.org/10.1021/acsapm.4c00831.

[8] Lin J, Feng X, Huang J, Liu Y, Xiao Y, Li Y, et al. Flexible AIE/PCM composite fiber with biosensing of alcohol, fluorescent anti-counterfeiting and body thermal management functions. Biosens Bioelectron 2025;267. https://doi.org/10.1016/j.bios.2024.116799.

[9] Geng L, Luo K, Lin Y, Li G, Cao Y, Zhao J, et al. Facile ester-based phase change materials synthesis for enhanced energy storage toward battery thermal management. Adv Sci 2025;12. https://doi.org/10.1002/advs.202413703.

[10] Cao S, Zhao X, Wang F, Wang J, Yang R. Experimental investigation on the thermophysical properties and solidification characteristics of n-octadecane in a spherical capsule. Case Stud Therm Eng 2024;64. https://doi.org/10.1016/j.csite.2024.105475.

[11] Yousefi E, Jaliliantabar F, Adam Abdullah A. Exploring the temperature-dependent thermal stability of nano-enhanced phase change materials: an experimental study using eicosane as the base material. In: Mater today proc, 107. Elsevier Ltd; 2022. p. 202–7. https://doi.org/10.1016/j.matpr.2023.10.008.

[12] Paul A, Baumhögger E, Dewerth MO, Dindar IH, Sonnenrein G, Vrabec J. Thermal conductivity of solid paraffins and several n-docosane compounds with graphite. J Therm Anal Calorim 2023;148:5687–94. https://doi.org/10.1007/s10973-023-12107-2.

[13] Annevelink CE, Sapp PA, Petersen KS, Shearer GC, Kris-Etherton PM. Diet-derived and diet-related endogenously produced palmitic acid: effects on metabolic regulation and cardiovascular disease risk. J Clin Lipidol 2023;17:577–86. https://doi.org/10.1016/j.jacl.2023.07.005.

[14] Jia M, Wang Y, Wang J, Qin D, Wang M, Chai L, et al. Myristic acid as a checkpoint to regulate STING-dependent autophagy and interferon responses by promoting N-myristoylation. Nat Commun 2023;14. https://doi.org/10.1038/s41467-023-36332-3.

[15] Zhang Y, Li W, Pei Q, Zhang X, Zhou Z, Xu S, et al. Effect of stearic acid coating on the flame propagation and reaction mechanism of AlH3. Fuel 2024;358. https://doi.org/10.1016/j.fuel.2023.130140.

[16] Lin N, Li C, Zhang D, Li Y, Chen J. Emerging phase change cold storage materials derived from sodium sulfate decahydrate. Energy 2022;245. https://doi.org/10.1016/j.energy.2022.123294.

[17] Li C, Li M, Li Y. Tailored calcium chloride hexahydrate as a composite phase change material for cold storage. J Energy Storage 2022;56. https://doi.org/10.1016/j.est.2022.105798.

[18] Shi L, Zhang J, Zhao M, Tang S, Cheng X, Zhang W, et al. Effects of polyethylene glycol on the surface of nanoparticles for targeted drug delivery. Nanoscale 2021;13:10748–64. https://doi.org/10.1039/d1nr02065j.

[19] Zhu G, Zou M, Luo W, Huang Y, Chen W, Hu X, et al. A polyurethane solid–solid phase change material for flexible use in thermal management. Chem Eng J 2024;488. https://doi.org/10.1016/j.cej.2024.150930.

[20] Harish S, Orejon D, Takata Y, Kohno M. Thermal conductivity enhancement of lauric acid phase change nanocomposite with graphene nanoplatelets. Appl Therm Eng 2015;80:205–11. https://doi.org/10.1016/j.applthermaleng.2015.01.056.

[21] Cai S, Ji J, Zhang X, Zhang C, Pan Z, Zhang C, et al. Development of bio-based flexible phase change materials utilizing lauric acid for battery thermal management systems. J Energy Storage 2024;86. https://doi.org/10.1016/j.est.2024.111382.

[22] Geng L, Xiao T, Jiang J, Luo K, Yan Y, Liu C. Wide temperature range phase change cold energy storage by using esterification between polyethylene glycol and lauric acid. Chem Eng J 2024;496. https://doi.org/10.1016/j.cej.2024.154005.

[23] Kuila C, Maji A, Murmu NC, Kuila T. Hexagonal boron nitride (h-BN) "a miracle in white": an emerging two-dimensional material for the advanced powered electronics and energy harvesting application. Compos B Eng 2025;301. https://doi.org/10.1016/j.compositesb.2025.112531.

[24] Zhou H, Uemura S, Feng Q, Sekino T, Kusunose T. Improvement of the anisotropic thermal conductivity of h-BN filled epoxy composites by changing the filler shape to spherical. J Mater Chem A Mater 2024;12:29923–31. https://doi.org/10.1039/d4ta06059h.

[25] Kang I, Kim H, Yoo H, Lee J. Synthesis of GPTMS-SiO2 nanofluid and its characterization for improving CO2 storage efficiency in saline aquifers: dispersion stability, rheological and interfacial behaviors. Mater Chem Phys 2025;343. https://doi.org/10.1016/j.matchemphys.2025.131010.

[26] Jilani W, Bouzidi A, Hamdi R, Al-Dossari M, Yahia IS, Guermazi H. Experimental investigations of DGEBA epoxy resin dispersed liquid crystal polymer systems for the development of new electronic devices. J Mol Liq 2024;395. https://doi.org/10.1016/j.molliq.2023.123923.

[27] Wang R, Geng L, Zhang X, Liang G, Zhao J, Liu C. Synthesis of flexible form stable phase change materials with in-situ formed porous TiO2 for personal thermal management. Chem Eng J 2025;505. https://doi.org/10.1016/j.cej.2025.159592.

[28] Geng L, Xiao T, Cao Y, Li G, Liang G, Liu C. Chinese tofu-inspired nanocuring: rapid UV-assembled phase change composites with mechanical-thermal synergy. Chem Eng J 2025;523. https://doi.org/10.1016/j.cej.2025.168321.

[29] Ramspoth TF, Flapper J, van den Berg KJ, Feringa BL, Harutyunyan SR. A highly efficient and sustainable catalyst system for terminal epoxy-carboxylic acid ring opening reactions. Green Chem 2024;26:3346–55. https://doi.org/10.1039/d3gc04301k.

[30] Levchik SV, Weil ED. Thermal decomposition, combustion and flame-retardancy of epoxy resins - a review of the recent literature. Polym Int 2004;53:1901–29. https://doi.org/10.1002/pi.1473.

[31] D'Eusanio V, Rombolà AG, Coralli I, Fabbri D, Tassi L, Marchetti A. Thermal degradation pathways in multi-component epoxy composites. J Anal Appl Pyrolysis 2025;189. https://doi.org/10.1016/j.jaap.2025.107107.

[32] Sainsbury T, Satti A, May P, Wang Z, McGovern I, Gun'ko YK, et al. Oxygen radical functionalization of boron nitride nanosheets. J Am Chem Soc 2012;134:18758–71. https://doi.org/10.1021/ja3080665.

[33] Mitran RA, Ioniță S, Lincu D, Berger D, Matei C. A review of composite phase change materials based on porous Silica nanomaterials for latent heat storage applications. Molecules 2021;26. https://doi.org/10.3390/MOLECULES26010241.

[34] Zhang X, Zhang Y, Wang X, Zhao J, Zou J, Sui X, et al. Composite phase change materials by confining polymers inside nanocarbon assemblies: a review. Next Energy 2025;7. https://doi.org/10.1016/j.nxener.2025.100281.

[35] Nagar S, Sreenivasa S. Polymer-based supporting materials and polymer-encapsulated phase change materials for thermal energy storage: a review on the recent advances of materials, synthesis, and characterization techniques. Polym Eng Sci 2024;64:4341–70. https://doi.org/10.1002/pen.26852.

[36] Scalfi L, Coasne B, Rotenberg B. On the gibbs-thomson equation for the crystallization of confined fluids. J Chem Phys 2021;154. https://doi.org/10.1063/5.0044330.

# Update

Journal of Materials Research and Technology
Volume 39, Issue , November - December 2025, Page 7548

DOI: https://doi.org/10.1016/j.jmrt.2025.11.044

Journal of Materials Research and Technology 39 (2025) 7548–7548

Contents lists available at ScienceDirect

Journal of Materials Research and Technology

journal homepage: www.elsevier.com/locate/jmrt

Corrigendum

# Corrigendum to 'Phase change material composites in a clay-like structure featuring GPTMS and butylated epoxy for heat buffering and thermal interface performance' [J Mater Res Technol Volume 39, (2025) Pages 5573–5581]

Sangwoo Kim [a], Wondu Lee [a], Taeyoon Hwang [a], Jinhyun Park [a], Nahyun Lee [a], Pei-Chen Su [c], Jooheon Kim [a,b,*]

[a] School of Chemical Engineering, Chung-Ang University, Seoul, 06974, Republic of Korea
[b] Department of Intelligent Energy and Industry, Graduate School, Chung-Ang University, Seoul, 06974, Republic of Korea
[c] School of Mechanical and Aerospace Engineering, Nanyang Technological University, 50 Nanyang Avenue, 639798, Singapore

The authors regret

< We requested a correction to the acknowledgments section of the paper, as we made an error.

Incorrect acknowledgments:

This research was supported by On-site Customized Personal Protection Technology Based on Multilayer Advanced Materials Program through the Korea Institutes of Police Technology (KIPoT) funded by the Korean National Police Agency & the National Fire Agency* (No. RS2025-02221259)

Acknowledgments requesting correction:

This research was supported by the National Research Foundation of Korea (NRF) grant funded by the Korea government (MSIT) (RS-2022-NR068145) and supported by Korea Institute for Advancement of Technology (KIAT) grant funded by the Korea Government (MOTIE) (RS-2025-02263458, HRD Program for Industrial Innovation). >

The authors would like to apologise for any inconvenience caused.

We sincerely regret that a significant error was made in the Acknowledgments section, which requires correction. We also apologise for requesting this amendment after submission. We are deeply grateful to the editorial office for their kind attention and efforts in accommodating this correction.

DOI of original article: https://doi.org/10.1016/j.jmrt.2025.10.218.
* Corresponding author. School of Chemical Engineering, Chung-Ang University, Seoul, 06974, Republic of Korea.
*E-mail address:* jooheonkim@cau.ac.kr (J. Kim).

https://doi.org/10.1016/j.jmrt.2025.11.044

Available online 6 November 2025
2238-7854/© 2025 The Author(s). Published by Elsevier B.V. All rights are reserved, including those for text and data mining, AI training, and similar technologies.